Surface-plasmon studies on Al (111) and Al (001) single-crystal surfaces using inelastic low-energy electron diffraction*

J. O. Porteus and W. N. Faith
Physics Division, Michelson Laboratory, China Lake, California 93555
(Received 24 March 1975)

Inelastic low-energy-electron-diffraction measurements on single-crystal Al (111) and Al (001) were made. The data required for comparison of the short-wavelength surface-plasmon dispersion on these two faces was obtained. Ultrahigh-vacuum procedures, including *in situ* sample cleaning and Auger analysis, were used to insure sample cleanliness. The elastic (00) beam energy profiles from Al (001) were measured over extensive ranges of energy and incidence angles in four azimuths. These profiles, which show abundant dynamical effects, were used to select conditions amenable to a kinematic analysis of the inelastic data. The inelastic data from Al (001), which is in the form of angular-selective loss profiles, is similar to that previously obtained from Al (111) except for an additional loss peak found on the former face. A close comparison of the energy positions of the surface-plasmon loss peak on the two faces, using simple conservation-law data analysis, shows the dispersion to be face dependent. The results of a more sophisticated kinematic analysis, which supports and quantifies this conclusion, are discussed briefly.

I. INTRODUCTION

The dispersion of short-wavelength surface plasmons, particularly in relation to the electronic structure of metal surfaces, is still an unresolved issue. Although extensive calculations have been reported,[1–7] adequate experimental information on well-characterized surfaces is lacking. It has been known for some time that certain contaminants have a pronounced influence on the energy required to excite surface plasmons.[8] However, Auger spectroscopy and similar methods now available for direct assessment of cleanliness have not previously been applied to this problem. Differences in surface crystallography may also alter the dispersion via resulting differences in the electron density profile at the surface. This unexplored effect, which requires well-defined surface structures for its observation, is the principal object of the present study. Because of the difficulty in preparing nominally clean single-crystal samples of suitable geometry, dispersion data based on high-energy electron forward scattering[9–12] has been restricted to polycrystalline films of undetermined structure. Results based on plasmon thresholds in the secondary electron yield[13] have also been limited to uncharacterized films. The method based on inelastic low-energy electron diffraction (ILEED),[14–16] on the other hand, is applicable only to well-defined structures. Here the signal is produced only by flat, ordered portions of the sample surface[17] which yield well-defined elastic low-energy electron diffraction (ELEED), thereby providing unequivocal identification of the pertinent crystallographic face. Until recently, however, ILEED measurements appropriate for a quantitative dispersion analysis[18] have been reported only for epitaxially prepared Al (111) surfaces in a paper[19] henceforth designated as I. The present paper extends I to sputter-cleaned Al (111) and Al (001) single-crystal surfaces, thus enabling a comparison of the surface-plasmon dispersion and lifetime (SPDL) on surfaces which differ either in method of preparation or in crystallographic orientation. It also provides a basis for a proposed study of the effect of ordered Na overlayers.[20] The work on the Al (001) surface has been coordinated with independent work in another laboratory[21] and with further development of procedures used to analyze ILEED data.[22]

Unfortunately, the intimate relationship between ELEED resonance maxima and ILEED loss spectra presents a formidable difficulty in extracting quantitative dispersion information from the raw data. Considerable progress has been made as a result of a concentrated theoretical effort with close experimental cooperation.[22,23] The major problem is to properly account for dynamical, or multiple-elastic, scattering effects. Criteria for obtaining kinematic data, i.e., data in which multiple-scattering effects may be neglected, have become increasingly restrictive with experience. It was shown previously, for example, that early results on Al (111) based on data in angular profile form must be discarded in favor of later results based exclusively on loss profiles.[23] More recent work[24] indicates, particularly in the case of Al (001) that the loss-profile data are more sensitive to dynamical influences than previously realized. This has necessitated a more restrictive selection of favorable ILEED measurement conditions based on peak positions in the elastic energy profiles. A complete analysis will be reported elsewhere.[22] The present paper is confined to a very elementary analysis, and is devoted mainly to a

description of the data base and experimental aspects of the study.

Following a brief review of theoretical considerations in Sec. II, in Sec. III we describe the apparatus and procedure used to prepare the clean, single-crystal surfaces. In Sec. IV A we present a comparison of plasmon loss-peak positions for the macroscopic single crystal vs epitaxial Al (111) surfaces, with the conclusion that no significant differences occur. In Sec. IV B we focus attention on single-crystal Al (001). An extensive survey of the (00) beam elastic energy profiles is first presented. This provides a basis for selecting the parameters for the ILEED data, which follows. In Sec. IV C we compare the surface-plasmon dispersion for the two different crystal faces, as obtained directly from conservation of energy and momentum. It is concluded that a consistent difference exists between these two sets of results. In Sec. V we present a summary of the work.

II. THEORY

The procedure for extracting the SPDL from ILEED measurements is basically as described in I and in the theoretical literature.[14,18] The analysis applied in the present paper is an elementary one based on the conservation-law model (CLM).[15,19] However, since the measurements have been aimed at the more sophisticated treatment given in the analytical paper,[22] the requirements, advantages, and recent improvements of this method will also be reviewed.

The ILEED process may be accurately regarded as a coherent two-step scattering of electrons having primary energy $E \sim 100$ eV, by a well-characterized, ordered surface. The steps, which may occur in either order, consist of (a) inelastic forward scattering, in which the electron loses energy w and excites a surface plasmon of equal energy $\hbar\omega_s(p_\parallel)$ and momentum $p_\parallel$ parallel to the surface, and (b) elastic diffraction in the back direction, corresponding to an ELEED resonance. The analysis is simplified considerably when (b) corresponds to specular (00) diffraction and (a) is restricted to electrons scattered into the plane of incidence. Thus, in the usual experimental arrangement, the source and detector, which determine the incidence and exit (polar) angles θ and θ', respectively, are coplanar with the surface normal. This plane or azimuth may be specified either by the crystallographic direction corresponding to the projected (on the surface) exit direction, or by the angle ϕ measured between the projected exit direction and a designated reference direction in the surface plane. With this two-dimensional scattering geometry it can be shown,[15] by invoking conservation of energy and conservation of momentum parallel to the surface, i.e., the CLM, that

$$p_\parallel = (\hbar^2/2m)^{-1/2}[(E-w)^{1/2}\sin\theta' - E^{1/2}\sin\theta]. \quad (1)$$

This equation applies to both diffraction-before-loss (DL) and loss-before-diffraction (LD) ordering of the two-step scattering. The relationship between plasmon momentum and measured experimental quantities permits evaluation of the surface-plasmon dispersion (SPD) via conservation of energy, i.e.,

$$\hbar\omega_s(p_\parallel) = w \ . \quad (2)$$

The intensity of scattered electrons may be presented as a function of any one of the three variables, E, θ', or w, with the remaining variables, including ϕ and θ, held constant. These three types of inelastic profiles are known as energy, angular, or loss profiles, respectively. Ideally, an intensity peak occurs in each profile at the point where Eqs. (1) and (2) are simultaneously satisfied. Each loss profile, for example, contains a surface-loss peak whose position w, together with the values of E, θ and θ' at which the profile was measured, provides $p_\parallel$ via Eq. (1) and $\hbar\omega_s(p_\parallel)$ via Eq. (2). Each loss profile thus provides one point on the SPD. Different loss profiles measured at different values of θ' provide different points, permitting in principal a determination of the entire SPD. In practice extreme values of $|p_\parallel|$ are excluded by experimental limitations. At small values of $|p_\parallel|$, inadequate angular resolution and, to a lesser degree, a large ELEED background, preclude exploration of the retardation region in detail. At large values of $|p_\parallel|$, the coherent inelastic signal becomes lost in the incoherent inelastic background. Values of E near the energy E_B of a strong peak in the elastic energy profile (ELEED intensity vs E) are the most favorable for ILEED measurements because of the large elastic scattering. From an experimental standpoint the value of $E \approx E_B + \hbar\omega_s$, where the LD process predominates, is especially favorable as a result of the relatively high ratio of ILEED to ELEED intensities.[19] The large variations of the elastic scattering with energy and angle associated with the elastic peaks can have an important influence on peak positions in the inelastic profiles. The failure to account for this effect is the chief limitation of the CLM method for determining the SPD. To be adequate in this respect, the analysis of ILEED requires a theory which can relate inelastic peak positions to elastic scattering characteristics. Also, determination of the surface-plasmon lifetime (SPL) requires a theory which provides inelastic peak widths. Because of its inability to provide information on intensities, such considerations are beyond the

scope of the CLM.

The method used in the analytical paper[22] is based on a previously described kinematical two-step model[14] which permits detailed calculation of intensities in the inelastic profiles. Inputs to calculations based on the model are (a) a kinematic representation of the elastic profile, (b) trial SPDs and (c) the SPL obtained from a dynamical analysis of observed peak widths in inelastic profiles. The final SPD is obtained by fitting theoretical to measured profiles. Loss profiles are used to present the inelastic signal, since it has been found that data in this form is least subject to dynamical scattering influences. Angular profiles are used only to determine the background arising from incoherent inelastic scattering. Further refinements of the analysis which are not incorporated in the CLM method include subtraction of the background, correction for overlap of the bulk-plasmon loss peak, and correction for instrumental resolution.[14]

Three conditions must be satisfied for the validity of the kinematic model analysis of the ILEED data. First, it must be possible to represent certain peaks in the elastic energy profiles by Bragg peaks. This is especially critical in the case of the LD process, where the diffraction condition depends on the scattering angle. In the analysis of Al (001), it became evident not only that the observed peaks must be relatively free from dynamical structure, but also that their energies must obey the kinematical relationship[22]

$$E_B = \cos^{-2}\theta\left[-V_0+\frac{\hbar^2}{2m}\left(\frac{\pi}{d}\right)^2 n^2\right] \tag{3}$$

over a range of θ corresponding to the range of scattering angles to be analyzed. Here, V_0 is the "inner potential" correction, d is the lattice spacing, and n is the order of the diffraction maximum. An extensive experimental study of the (00) elastic profile is required in order to find suitably large ranges of E and θ where these conditions are satisfied. Examples of raw elastic profiles used in this study are presented in Sec. V. The second requirement is that the SPD determined on the basis of data sets corresponding to different diffraction conditions, i.e., different E_B, E, θ, and ϕ, be consistent. The SPDL of the semi-infinite solid is assumed to be of the form

$$\hbar\omega_s(p_\parallel) = \hbar\omega_s + C_1 p_\parallel + C_2 p_\parallel^2 , \tag{4a}$$

$$\Gamma_s(p_\parallel) = \Gamma_s + D_1 p_\parallel , \tag{4b}$$

where Eqs. (4a) and (4b) express the real and imaginary (damping or lifetime) parts, respectively. Regions of ambiguity of all dispersion constants $\hbar\omega_s$, C_1, C_2, Γ_s, and D_1 must intersect for all data sets in order for the analysis to be regarded as successful. The third requirement is that loss profiles computed from a rigorous dynamical model be essentially equivalent to those given by the kinematic two-step model. Since use of the dynamical model places heavy demands on computer time, only a very limited application of this requirement is possible in practice.

III. EXPERIMENTAL PROCEDURE

Except for modifications required for the different method of sample preparation used here, the experimental apparatus and procedures are identical to those described in I. The diffractometer uses an emission-stabilized tungsten-filament source, whose intensity characteristics are exemplified in Fig. 1. The detector is a moving Faraday cylinder equipped with 2° collimating apertures and a retarding field analyzer, which, together with the source, gives a measured energy spread of $\lesssim 1$ eV. The detector signal S, consists of the dc-amplified current due to electrons having energy greater than the retarding potential E_r. For elastic data, unnormalized energy profiles are obtained by direct analog plotting of S, with E_r set to exclude all but elastically scattered electrons. Consistency of nonspecular beam energies and angles with the bulk lattice spacing is used to establish the energy origin. The intensity normalization, which would be extremely tedious in this situation, is omitted, since the pertinent information on peak structure and position is directly available from the raw data. For inelastic data, several scans are performed at each fixed collector angle θ' by record-

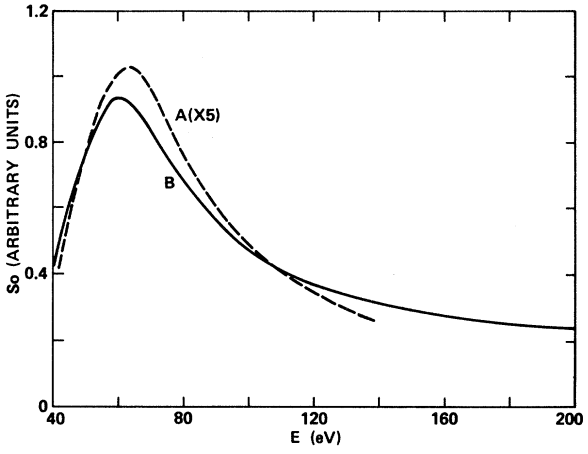

FIG. 1. Signal S_0 from the source as a function of the energy E of the electron beam measured with the detector facing the source. Curves A and B, which differ by a nominal factor of 5 change in intensity, characterize different operating conditions used to obtain the elastic energy profiles presented in Figs. 3–6.

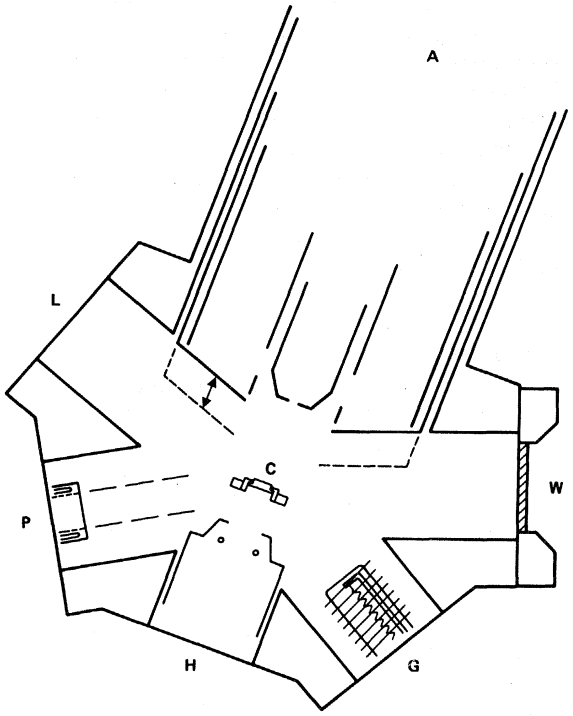

FIG. 2. Sample preparation chamber viewed toward the gun end of the diffractometer. The sample C may be rotated to face either the Auger analyzer A or the sputter gun P. The Auger analyzer may be moved in the directions of the arrows for focusing.

ing S on digital magnetic tape as E_r is repeatedly stepped through the desired range. Average inelastic intensities $I = dS/dw$ and their standard deviations σ_I are computed directly from the tape using Eqs. (I1) and (I2), respectively.[25] Included in the computation are normalization of S using the source signal S_0 (Fig. 1), an obliquity correction for variation of the active sample dimension, and a conversion of E_r to w based on the peak position of the elastic component from independently measured inelastic profiles.[19] Data points with error bars are machine plotted either as angular or as loss profiles.

The sample preparation chamber shown in Fig. 2 of I has been replaced by that shown in Fig. 2 of the present paper. Except for location, the electron bombardment heater H, ion gauge G, and window W remain unchanged. New items include the Auger cylindrical mirror analyzer A with integral electron gun, sputter gun P, and argon inlet L. Focusing motion for A is provided by a concentric bellows and screw, which permit translation along the analyzer axis as indicated. Motion of the sample C is restricted here to translation along, and 360° rotation about the chamber axis, which lies along the sample surface and normal to the plane of the figure.

A modification of the pumping system enables rapid and complete evacuation of the argon sputtering gas. The original Orb-ion pump has been supplemented with a 60-liter/sec noble-ion pump connected through a 4-in. bakeable valve. To achieve adequate ultrahigh vacuum during the measurement interval, the Orb-ion pump and its attendant cooling are not normally turned on until after sputter-cleaning is completed and the system has been pumped into the low 10^{-8}-Torr range. Immediately following this and prior to annealing, the bakeable valve is closed. The noble-ion pump is then turned off and its magnets removed to provide a virtually field-free measurement space. Since the pumping speed of the noble pump working alone during bakeout is inadequate to handle the gas load, the Orb-ion pump is also operated at this time, but without cooling.

The method used to prepare the clean Al single-crystal surfaces is identical to that used in a previous study.[20] The crystal is first reduced to the form of a $\frac{3}{8}$-in.-diam$\times$0.060-in.-thick disk using a spark cutter. The surface is then mechanically ground and polished to within 0.01° of the desired crystal planes as measured by an x-ray goniometer which accommodates the polishing jig. To ensure removal of damaged material and most of the surface oxide, each crystal is electropolished in perchloric-acid–ethanol solution immediately before placing in vacuum. Final cleaning is done in the sample preparation chamber by alternate one-hour intervals of ion bombardment and annealing at 500 °C. Initially, less than ten hours of this treatment are normally required to reduce all resolvable contaminant Auger peaks occurring below 1400 eV (mainly O, C, and Nb) to levels $<0.1\%$ of the intensity of the 67-eV Al peak, as observed with a 2-keV probe beam. Subsequent cleaning performed prior to each set of measurements requires two hours or less. As a precaution against contamination during sputtering, the sample is provided with a recessed shoulder which accommodates the mounting frame. As an added precaution, the mounting frame is made of high-purity Al to prevent direct contact with the Nb sample palette described in I. The sample is allowed to cool to 100 °C or less before any measurements are made. Auger analysis and LEED data repetition after measurement periods extending up to four hours in a vacuum of 2×10^{-10} Torr or better indicate no detectable increase in contamination levels.

IV. EXPERIMENTAL RESULTS AND DISCUSSION

A. Single-crystal Al (111)

In order to permit comparison of earlier results from epitaxially prepared Al (111) with those from

TABLE I. Comparison of peak positions in loss-profile data from Al (111) macroscopic single-crystal (w_m) with those from Al (111) epitaxial samples (w_e): $\langle 11\bar{2}\rangle$ azimuth, $\theta = 15°$, $E_B = 49$ eV.

E (eV)	θ' (deg)	Surface $w_m - w_e$ (eV)	(±) (eV)	Bulk $w_m - w_e$ (eV)	(±) (eV)
50	8	0.0	0.2	0.0	0.2
	10	0.0	0.1	0.0	0.2
	12	−0.1	0.1		
	13	0.0	0.1	0.0	0.2
	14	0.0	0.4		
	15	−0.3	0.4		
	16	0.4	0.8		
	17	0.0	0.2	0.2	0.2
	18	0.0	0.1	0.1	0.2
	19	−0.1	0.1	0.0	0.2
	20	−0.1	0.1	0.0	0.2
	22	−0.2	0.1	0.0	0.3
	24	−0.2	0.2	−0.1	0.2
	26	0.1	0.2	−0.1	0.2
	28	−0.2	0.4	0.2	0.4
60	8	0.4	0.2		
	10	0.0	0.1		
	12	0.0	0.1		
	13	−0.1	0.1		
	14	−0.1	0.2		
	15	−0.2	0.3		
	16	−0.1	0.3		
	17			−0.2	0.2
	18			−0.2	0.2
	19			−0.1	0.2
	20			−0.3	0.2
	22			−0.1	0.2
	24			−0.1	0.3

the corresponding surface of a macroscopic single crystal, data on the latter type of sample was taken under conditions corresponding to those reported in I. Elastic energy profiles of the (00) beam measured in the $\langle 11\bar{2}\rangle$ azimuth at $\theta = 15°$ and $\theta = 25°$, 40 eV $\leq E \leq$ 140 eV, agree with those given in Fig. I6 to within the instrumental reproducibility. Likewise, in the $\langle 1\bar{1}0\rangle$ azimuth at $\theta = 15°$, a limited scan (40 eV $\leq E \leq$ 100 eV) shows satisfactory agreement with Fig. I7. Direct comparison of the nonspecular beam profiles is not possible because of double positioning of crystallites in the epitaxial film, whereas, in the case of the (00) beam, reciprocity provides sixfold symmetry of the intensity.[19] We conclude that, aside from the double positioning, relative ELEED intensities show no significant departure of the epitaxially prepared samples from the characteristics of a macroscopic clean single crystal.

ILEED profiles were also measured under conditions corresponding to Figs. I9 and I10, i.e., $\langle 11\bar{2}\rangle$ azimuth, $\theta = 15°$, $E = 50$, 60 eV. Except for a significantly lower incoherent background with the present sample, the two sets of data are in remarkably good agreement. A comparison of loss-profile results is given in Table I, where the differences $w_m - w_e$ between loss peak positions measured on the macroscopic and epitaxial samples are listed for both surface and bulk plasmons, together with uncertainties. In the case of the surface plasmon, the difference exceeds the uncertainty limits, which represent roughly 90% probability, in only 2 out of 22 situations. For the bulk plasmon the uncertainty is exceeded in only one situation. Thus it can be concluded that to within the accuracy of present measurements the ILEED characteristics, and hence the SPDL, are independent of which method of sample preparation is used. On this basis we shall consider the results of I as representative of clean single-crystal Al (111) in comparing with the results of Al (001) which follow.

B. Single-crystal Al (001)

The Al (001) surface has fourfold symmetry, with ELEED beams occurring at integral order positions in a square reciprocal net. In the convention used here, the $\langle 10\rangle$ and $\langle 01\rangle$ directions of the net correspond to the $\langle 100\rangle$ and $\langle 010\rangle$ crystallographic directions, or to the azimuths $\phi = 0°$ and 90°, respectively. Selecting the optimum conditions for the ILEED study of Al (001) differs somewhat from that described in I in that theoretical considerations now tend to override signal-to-noise considerations, particularly those regarding the selection of θ discussed in Sec. IV B of I. In accordance with Sec. II above, a greater emphasis is now placed on excluding dynamical situations via evaluation of elastic energy profiles, and somewhat less emphasis is placed on maximizing the prominence of the surface-loss peak.

Elastic energy profiles of the (00) beam have been recorded for 40 eV $\leq E \leq$ 200 eV, $9° \leq \theta \leq 29°$ ($\Delta\theta = 2°$) in each of the following azimuths: $\langle 100\rangle$ ($\phi = 0°$), $\langle 310\rangle$ ($\phi = 18.4°$), $\langle 210\rangle$ ($\phi = 26.6°$), and $\langle 110\rangle$ ($\phi = 45°$). Selected examples, which illustrate the problem of finding Bragg-like peaks suitable for a kinematic analysis, are presented in Figs. 3–6. Figures 3 and 4 present the complete set of elastic energy profiles for the $\langle 100\rangle$ azimuth. The prominent peak near $E = 70$ eV appears to be relatively free of dynamical structure in the range $9° \leq \theta \leq 15°$ and again in the range $21° \leq \theta \leq 29°$. However, a comparison with Bragg peak positions based on Eq. (3), with V_0 chosen for the best fit[22] (see also captions for Figs. 3–6), shows Bragg-like behavior only in the former range. The peak position in the latter range is nearly independent of θ; the intensity is in fact merely redistributed between adjacent peaks as θ is varied. The strong peak near $E = 140$ eV also is inadequately described

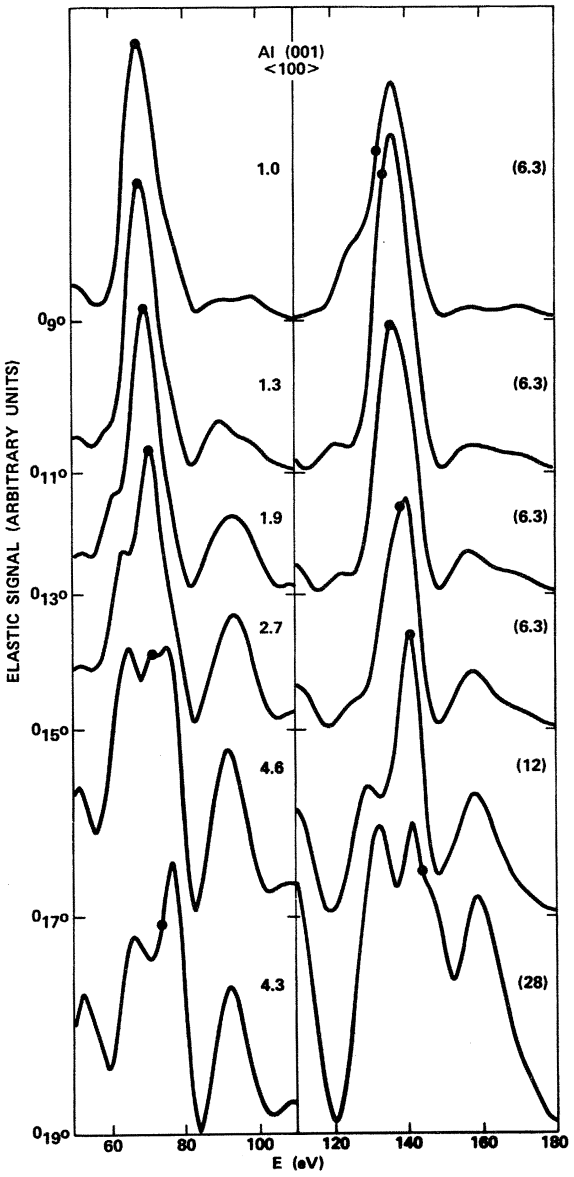

FIG. 3. Unnormalized elastic energy profiles of the (00) beam from Al (001) in the ⟨100⟩ azimuth for $9° \leq \theta \leq 19°$. Positions of the $n=3$ and $n=4$ Bragg peaks (solid circles) are based on Eq. (3) with $V_0=15$ eV. Relative scale factors based on the profile at the upper left are given to the right of each curve. Parenthesized scale factors include the nominal factor-of-5 intensity ratio between curves A and B of Fig. 1. Normalization curves B or A apply, respectively, depending on whether the scale factor is or is not enclosed in parentheses.

by Eq. (3), except in the range $11° \leq \theta \leq 17°$.

Figure 5 shows elastic energy profiles at small θ for the ⟨310⟩ azimuth. The peak near 70 eV shows nearly Bragg-like positioning for $9° \leq \theta \leq 17°$, approaching the corresponding situation in the ⟨100⟩ azimuth. The strong peak near 140 eV, on the other hand, is again somewhat less favorable in this respect. Both peaks show considerable scatter about positions based on Eq. (3) for $\theta > 19°$, i.e., for angles greater than those shown in Fig. 5. As the azimuth angle is further increased toward $\phi = 45°$, the situations generally appear less favorable. In the ⟨110⟩ azimuth (Fig. 6), the 70-eV peak position is very dynamical even at small values of θ, while the approximately kinematic θ range of the 140-eV peak is extremely limited. From these results it would appear that the peak near 70 eV, $\theta \leq 15°$, $\phi = 0°$ or 18.4°, is the most favorable for kinematic ILEED analysis. The case of the same peak at $\theta \simeq 25°$, $\phi = 0$, on the other hand, provides an example of an unfavorable, dynamical situation. The peak near 140 eV, $\phi = 0°$ or 18.4°, offers favorable possibilities at

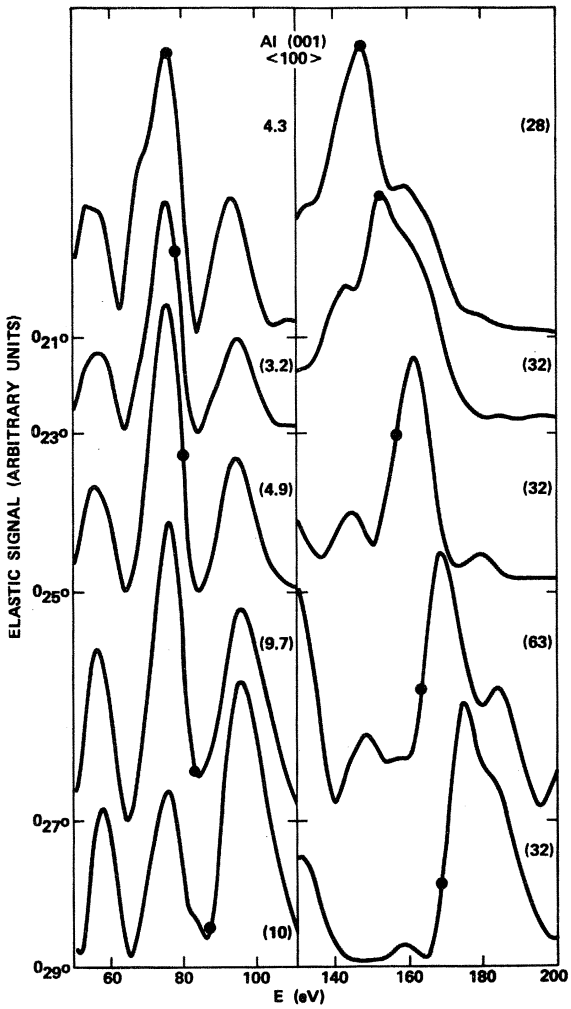

FIG. 4. Unnormalized elastic energy profiles of the (00) beam from Al (001) in the ⟨100⟩ azimuth for $21 \leq \theta \leq 29°$. Positions of the $n=3$ and $n=4$ Bragg peaks (solid circles) are based on Eq. (3) with $V_0=15$ eV. Relative scale factors are based on Fig. 3 and have the same significance.

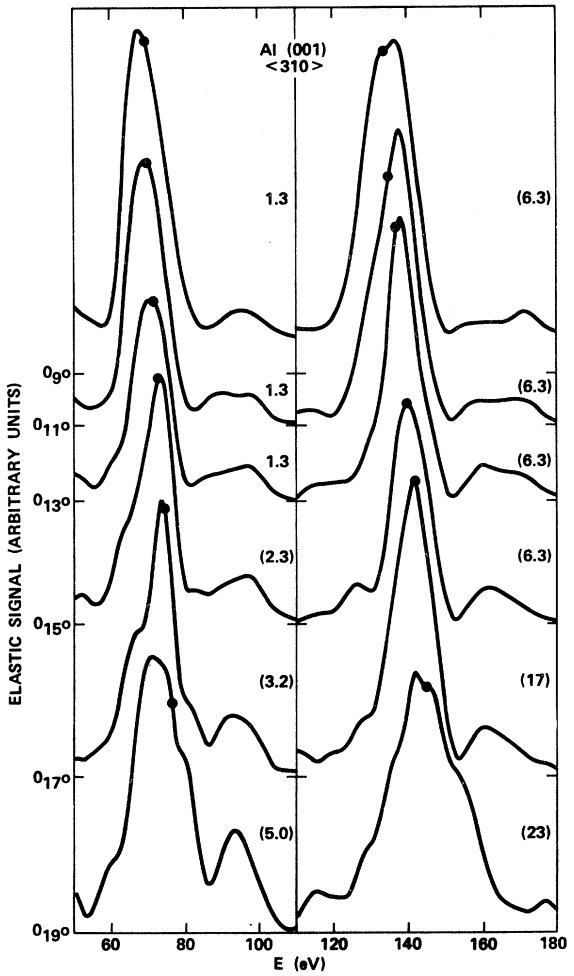

FIG. 5. Unnormalized elastic energy profiles of the (00) beam from Al(001) in the ⟨310⟩ azimuth for $9° \leq \theta \leq 19°$. Positions of the $n=3$ and $n=4$ Bragg peaks (solid circles) are based on Eq. (3) with $V_0=13$ and 14 eV, respectively. Relative scale factors are based on Fig. 3 and have the same significance.

a higher energy.

A list of the ILEED data, showing values or ranges of parameters, is given in Table II. The angles ϕ and θ and the Bragg peak were selected largely on the basis of the above considerations regarding the elastic energy profiles. Values of E were generally chosen to include the observed elastic peak energy E_B, where the DL process dominates, and also a value several eV above E_B, where the LD process dominates. Dynamical structure on the high-energy side of the peak dictates how large the latter E value can be made without encroaching on kinematic approximation of the elastic interaction. In the case of coarse-grid data ($\Delta\theta'_{max}=2°$, $\Delta w=0.4$ eV), the θ' range is made large enough to determine the incoherent inelastic background correction. The w range, on the other hand, is sufficient to include both surface- and bulk-loss peaks for evaluation of peak shifts due to overlap. In the case of fine-grid profiles ($\Delta\theta'_{max}=1°$, $\Delta w=0.1$ eV), these ranges have been compressed to encompass only the coherent signal from the surface plasmon. This allows correspondingly longer measurement times and closer data spacings, which permits more precise determination of peak positions as described in I.

Series of the coarse-grid loss profiles are presented in Figs. 7–12. Data points, including standard deviations, are shown connected by smooth curves. Figures 7 and 8 represent the conditions $\phi=0$, $\theta=12°$, with $E=E_B=69$ eV, and $E=E_B+7$ eV $=76$ eV ($n=3$), respectively. These two figures are approximately analogous to Figs.

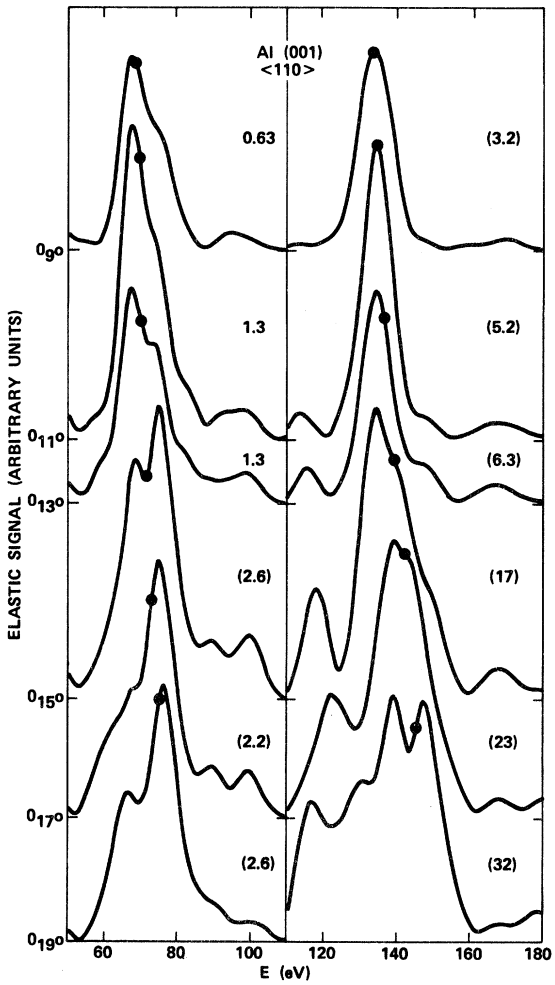

FIG. 6. Unnormalized elastic energy profiles of the (00) beam from Al(001) in the ⟨110⟩ azimuth for $9° \leq \theta \leq 19°$. Positions of the $n=3$ and $n=4$ Bragg peaks (solid circles) are based on Eq. (3) with $V_0=14$ eV. Relative scale factors are based on Fig. 3 and have the same significance.

TABLE II. List of inelastic data on Al (001) surface.

Az	ϕ (deg)	θ (deg)	E_B (eV)	E (eV)	θ' (deg)	$\Delta\theta'_{max}$ (deg)	w (eV)	Δw (eV)
⟨100⟩	0	12	69	69, 76	3–23	2	7–18	0.4
⟨100⟩	0	12	69	69, 76	4–13	1	9.5–11.5	0.1
⟨100⟩	0	15	140	132, 138, 144, 148	0–30	2	7–18	0.4
⟨100⟩	0	25	76	70, 76, 82	10–40	2	7–18	0.4
⟨100⟩	0	25	161	155, 161 167, 171	10–40	2	7–18	0.4
⟨100⟩	0	25	161	161, 167	16–24	1	10–12	0.1
⟨310⟩	18.4	13	71	71, 78	2–24	2	7–18	0.4
⟨310⟩	18.4	13	71	71, 78	4–13	1	9.5–11.5	0.1
⟨210⟩	26.6	15	140	134, 140, 146, 150	0–30	2	7–18	0.4

I9 and I10 with regard to the respective predominance of the DL and LD processes, and show similar dependences of peak intensities on θ'. Generally, the surface-loss intensity is greater for $\theta' < \theta$. This can be explained in part by the fact that the spherical surfaces of constant electron energy in k space are more nearly parallel to the sample surface when $\theta' < \theta$, which means that a greater number of plasmon states are included within the acceptance angle of the collector.[26] However, the reason for the large intensity asymmetry about $\theta' = \theta$ in the LD situation, e.g., Fig. 8, is not entirely clear.[27]

The SPD is evident in the shift of the surface-loss peak ($w \simeq 10$–12 eV) to higher w as $|p_{\parallel}|$ increases in accordance with Eq. (1). The bulk-loss peak ($w \simeq 14$–16 eV) undergoes a similar shift which is less simply related to the bulk-plasmon dispersion.[19] Also associated with the increase in $|p_{\parallel}|$ is a decrease of the surface-plasmon signal due to increased damping. Correspondingly, the position of the surface loss is more strongly influenced, and eventually dominated by the incoherent background. The influence of the overlapping bulk-plasmon peak may also be important, particularly for $\theta' > \theta$ in the LD-dominant situation where the relative intensity of the surface loss peak is especially low.

The presence of extra loss peaks must also be considered. Such peaks may originate from (a) dynamical effects, (b) ILEED from higher-order elastic beams, or (c) one-electron excitations. Experience from Al(111) indicates that the first type of extra peak, which is more prominently displayed in the angular-profile data, appears in the loss-profile data only at angles well away from the specular direction.[18,19] Probable examples are seen in Fig. 7 at $w \simeq 12.5$ eV in the $\theta = 5°$ and 23° profiles. The possibility that extra peaks of the second type are involved here cannot be definitely eliminated. However, their occurrence within the range of the figures is unlikely at these

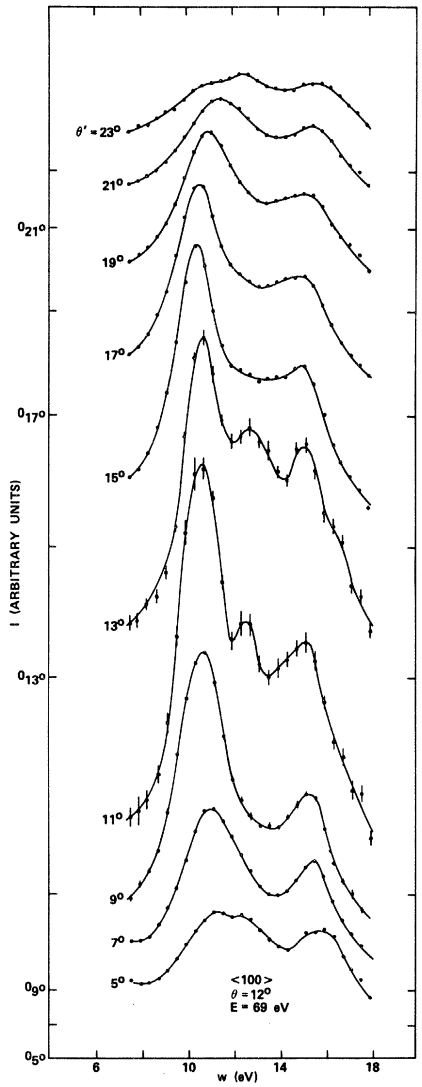

FIG. 7. Coarse-grid energy-loss profiles from Al (001) measured at a 69-eV Bragg-like peak at $\theta = 12°$. Displaced zero levels are indicated by tick marks along the vertical axis. Error bars for coarse-grid data represent standard deviations based on 16 repetitive scans.

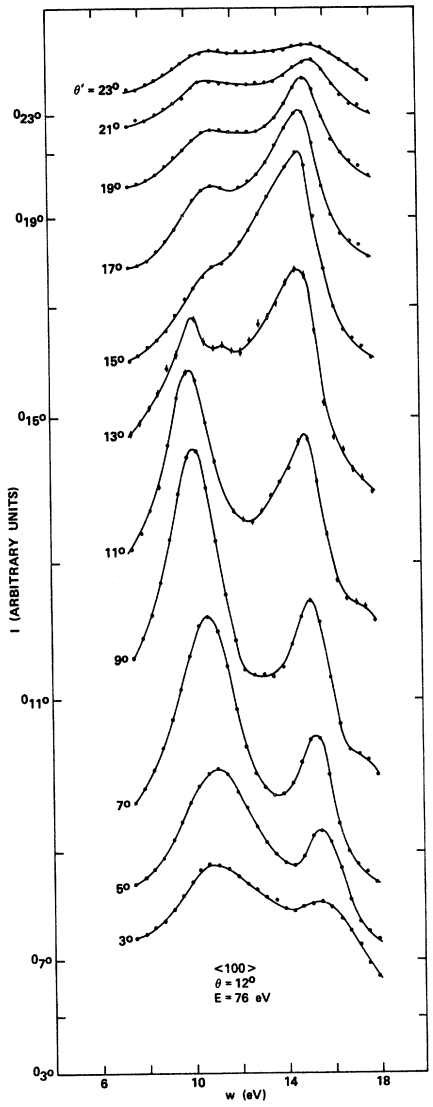

FIG. 8. Coarse-grid energy-loss profiles from Al (001) measured at 7 eV above a 69-eV Bragg-like peak at $\theta = 12°$.

primary energies, where the angular separation of elastic beams is relatively large. A probable example of the third type of peak is found in Fig. 7 at $\theta' = 11°$ and 13°, and in Fig. 8 at $\theta' = 13°$, lying between the surface- and bulk-loss peaks. The near-specular extra peak has also been observed by Wendelken, who used a differential-type analyzer.[21] This peak did not appear in our data from Al (111), which implies that the state of the excited electron and/or the excitation probability have a pronounced surface dependence. The restriction to near-specular angles indicates a value of $|p_{\parallel}|$ which is very small compared to that of the primary electron. This favors a one-electron type of excitation as opposed to a collective mode.

Increasing θ from 12° to 25° and compensating for the change in E_B yields Figs. 9 and 10, which are otherwise analogous to Figs. 7 and 8, respectively. The nonspecular extra peaks are especially prominent here, as might be expected in view of the relatively dynamical elastic profile in this situation. The near-specular extra peak is again in evidence in both figures. Changing the azimuth from $\phi = 0$ to $\phi = 18.4°$, but leaving θ and E nearly the same, transforms Fig. 8 into Fig. 11. Here an extra peak is seen at $\theta' = 4°$, with little evidence of the near-specular peak, although the latter is weak but still visible in the corresponding data at $E = E_B$ in this azimuth. Figure 12 presents an example of loss profiles at $\phi = 0°$ associated with the higher-energy ($n = 4$) Bragg peak, i.e., at $E = E_B + 6$ eV = 167 eV. The near-specular peak is virtu-

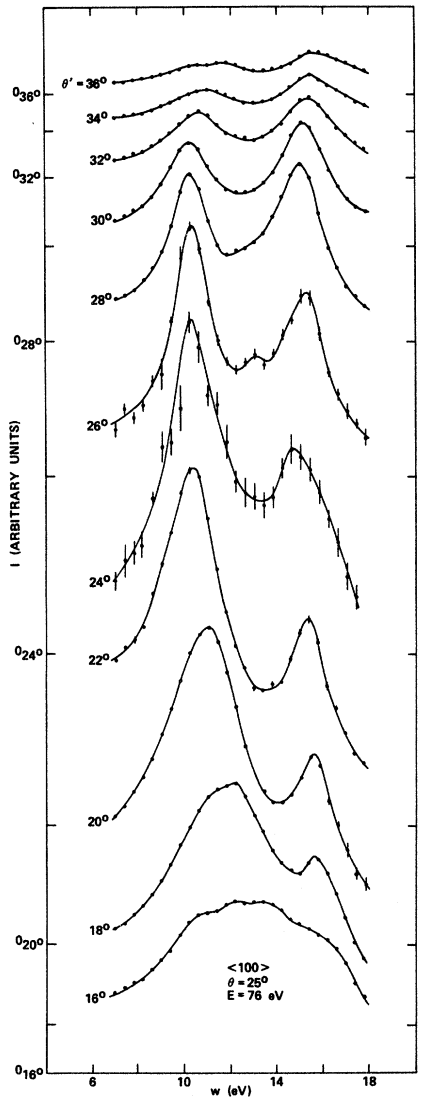

FIG. 9. Coarse-grid energy-loss profiles from Al (001) at a 76-eV elastic peak at $\theta = 25°$.

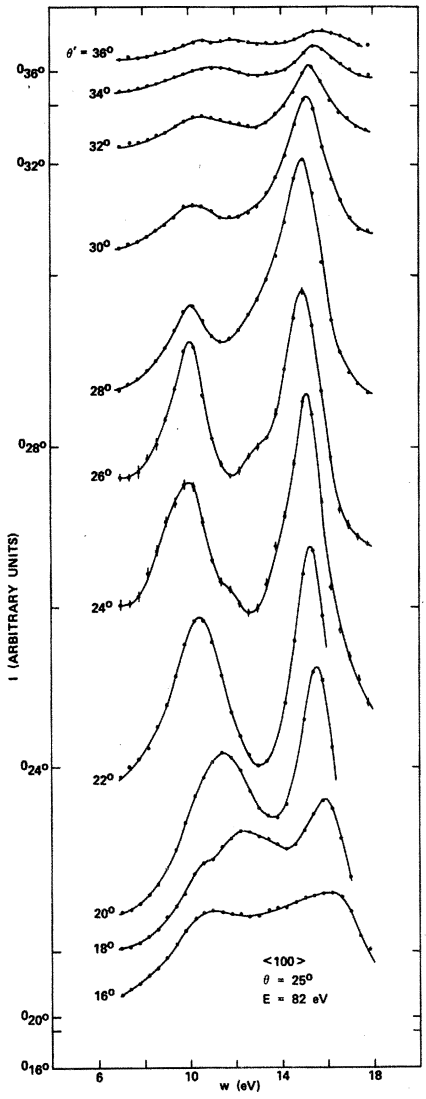

FIG. 10. Coarse-grid energy-loss profiles from Al (001) measured at 6 eV above a 76-eV elastic peak at $\theta = 25°$.

ally absent, both at this energy and at $E = E_B$, although multiple nonspecular peaks are evident in the DL situation. Other data involving the $n = 4$ Bragg peak are similar in this respect. The general suppression of the near-specular peak at the higher primary energies is an additional argument against its possible dynamical origin.

Figures 13–15 present examples of fine-grid profiles corresponding to Figs. 7, 8, and 12, respectively. The small extra peak in Fig. 8 at $\theta' = 13°$, $w = 11.4$ eV is again observed in Fig. 14. A peculiarity which is clearly seen in Fig. 15 is a shifting of the surface-loss peak to lower energies as θ' decreases from the specular direction. This effect is attributed partly to the incoherent inelastic background, which tends to dominate the coherent signal at smaller $|p_{\parallel}|$ as E is increased higher above the surface plasmon threshold $\hbar\omega_s$. Dynamical effects may play an important role here, however, especially since the elastic energy profile in this case is relatively dynamical.

C. Comparison of SPD on different crystal faces

By applying the CLM via Eqs. (1) and (2), as discussed in Sec. II, points on the SPD may be obtained from each set of loss profiles measured at a given ϕ, θ, and E. Examples of SPDs derived from data listed in Paper I and Table II of the present paper are presented in Figs. 16 and

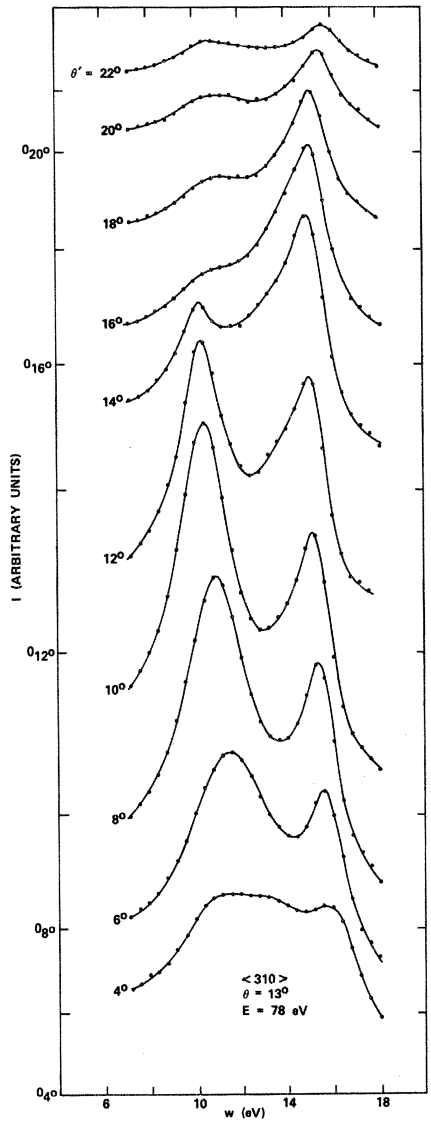

FIG. 11. Coarse-grid energy-loss profiles from Al (001) measured at 7 eV above a 71-eV Bragg-like peak at $\theta = 13°$ in the ⟨310⟩ azimuth.

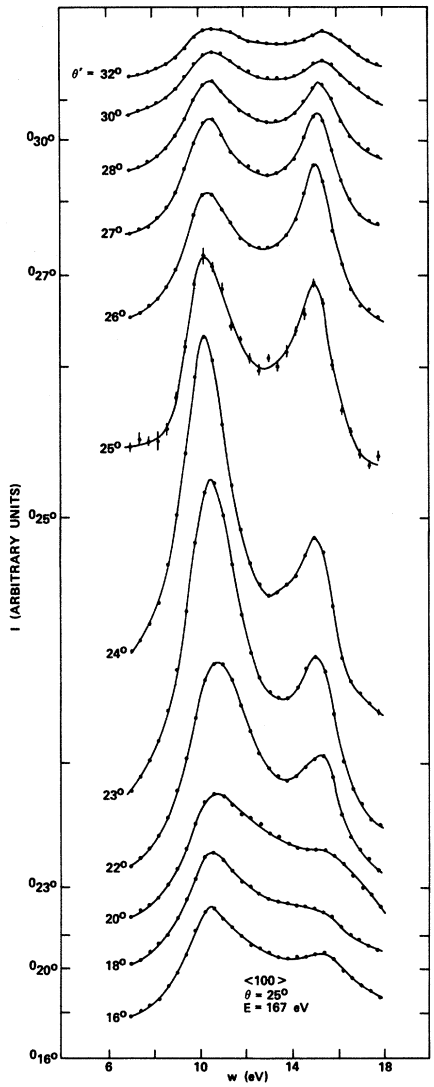

FIG. 12. Coarse-grid energy-loss profiles from Al (001) measured at 6 eV above a 161-eV Bragg-like peak at $\theta = 25°$.

17. In Fig. 16, where $E \simeq E_B$, the DL process dominates, while in Fig. 17, where $E > E_B$, the LD process dominates. The left-hand side of both figures represents the Al (001) surface, and the right-hand side Al (111), with opposite panels representing similar values of θ and E. A comparison is thus provided of the SPD measured under similar experimental conditions on the two surfaces. The vertical location of each point in the figures indicates the position w of a surface-loss peak in a loss profile, as measured to the center of a Lorentzian fitted to the peak. To achieve maximum precision, fine-grid data were used where available in preference to coarse-grid data. Vertical error bars represent the uncertainty in w with approximately 90% probability limits. No correction has been made for incoherent background or peak overlap. Uncertainty in in the relative horizontal location of the points is governed almost entirely by the θ' uncertainty ($\lesssim 0.2°$).

Although Figs. 16 and 17 show differences between individual panels, certain general features are displayed consistently. One such feature is the ultimate positive character of the SPD, i.e., $\hbar\omega_s(p_\parallel)$ tends to increase with $|p_\parallel|$ when $|p_\parallel|$ is sufficiently large. The combined effects of incoherent background and dynamical influences, which cause the SPDs to appear to bend down at larger $|p_\parallel|$ in certain cases, have already been discussed in connection with Fig. 15. The apparent asymmetry of the SPDs about $p_\parallel = 0$ is inadmissable on physical grounds, since the surface is symmetrical with respect to plasmon propagation in opposite directions. An apparent displacement toward $p_\parallel < 0$, which is most evident near $p_\parallel = 0$ in Fig. 17, may be attributed in part to the overlap of the bulk-loss peak. This has an increasing tendency to raise the apparent energy of the surface loss as θ' increases in the vicinity of $\theta' = \theta$ because of the rapidly diminishing relative intensity of the surface loss in this region. Additional asymmetry which is dispersion dependent can be explained by the two-step model.[28,29] This, together with the individual differences between data sets, emphasizes the need for an analysis based on a more sophisticated model.

Comparison of results from the two crystal faces in Fig. 17 shows a consistently lower SPD for the Al (001) face near $p_\parallel = 0$. It has been pointed

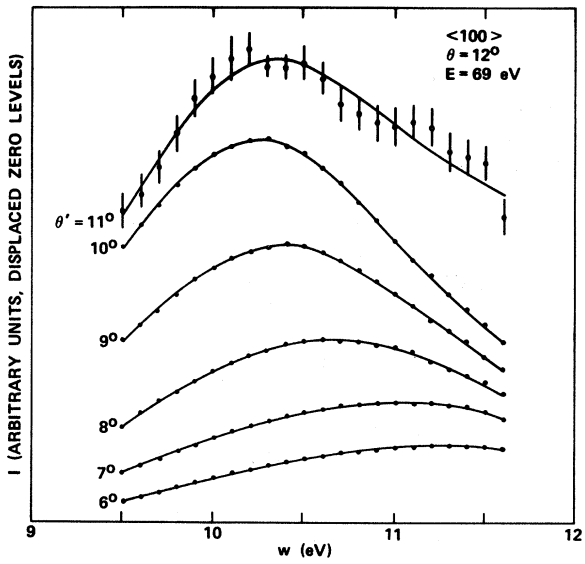

FIG. 13. Fine-grid energy-loss profiles corresponding to Fig. 7. Error bars for fine-grid data represent standard deviations based on 64 repetitive scans.

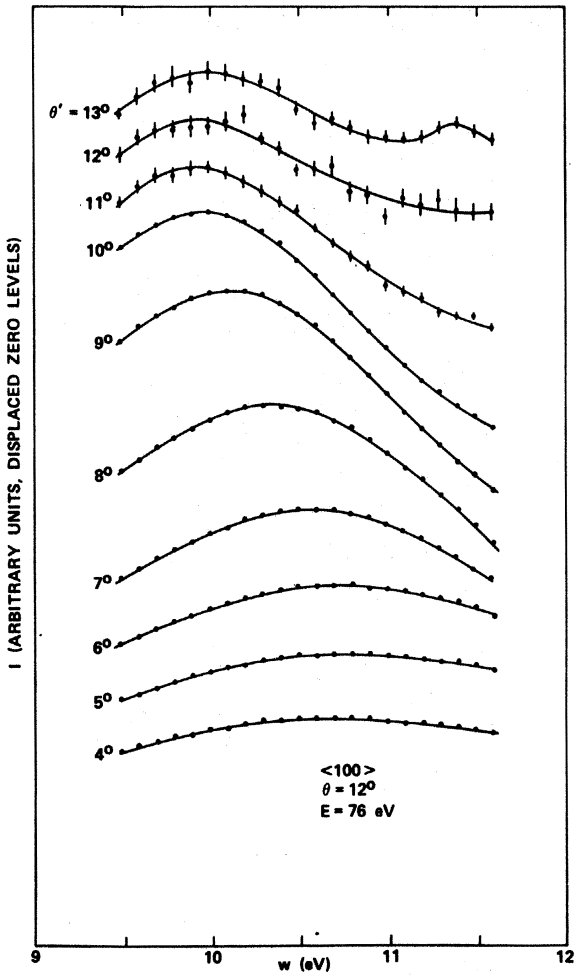

FIG. 14. Fine-grid energy-loss profiles corresponding to Fig. 8.

out[29] that diffraction effects can lower the apparent SPD as derived from the CLM as $\theta' \to \theta$, unless the LD process actually dominates, i.e., unless $E - E_B$ is sufficiently large. The examples from Al(001) in Fig. 17 do in fact represent values of $E - E_B$ which are 2–6 eV lower than the 10-eV value represented by the examples from Al(111). In spite of this, the available evidence does not support a significant dependence of $\hbar\omega_s(p_\parallel)$ on E. For example, no significant difference exists between the $E = 144$ eV "worst case" and $E = 148$ eV ($E_B = 140$ eV) panels of Fig. 17 near $p_\parallel = 0$. Likewise, the $\phi = 0$, $\theta = 25°$, $E = 171$ eV ($E_B = 161$ eV) data is in excellent agreement with the results presented in Fig. 17 for $E = 167$ eV. Also, the data at $\phi = 26.6°$, $\theta = 15°$, $E = 145$ and 150 eV ($E_B = 140$ eV) are in good agreement. In Fig. 16, the vertical differences between the SPDs from the two faces are smaller, but still significant. The most kinematical situation, $\phi = 0$, $\theta = 12°$, $E = 69$ eV, it will be recalled, also contains a relatively strong, extra loss peak near $\theta' = \theta$. The resulting overlap is partially responsible for the larger value of $\hbar\omega_s(p_\parallel)$ near $p_\parallel = 0$ in this case. With allowance for the influence of the extra loss peak, the evidence for the face dependence of the SPD is entirely consistent.

Unfortunately, it is impractical to proceed beyond a qualitative demonstration of the face dependence on the basis of the CLM because of the neglected effects of diffraction, background and overlap, and the resulting differences between the various data sets exhibited in Figs. 16 and 17. By simulating the effects peculiar to each measurement situation, the kinematic two-step model is capable of arriving at a quantitative relationship consistent with all data sets. However, this relationship may not be entirely unique. Analysis of the present and other available data[21] on Al(001) admits both[22]

$$\hbar\omega_s(p_\parallel) = 10.2(\pm 0.1) + 1.5(\pm 0.5)p_\parallel + 0(+2)p_\parallel^2 \tag{5a}$$

and

$$\hbar\omega_s(p_\parallel) = 10.4(\pm 0.1) - 2(\pm 1)p_\parallel + 9(\pm 3)p_\parallel^2 . \tag{5b}$$

In either case,

$$\Gamma_s(p_\parallel) = 1.2(\pm 0.5) + 1(\pm 0.5)p_\parallel . \tag{5c}$$

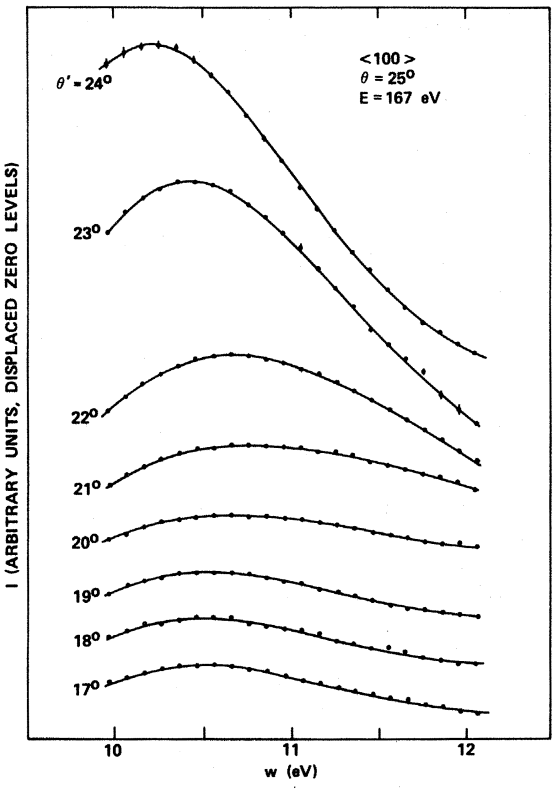

FIG. 15. Fine-grid energy-loss profiles corresponding to Fig. 12.

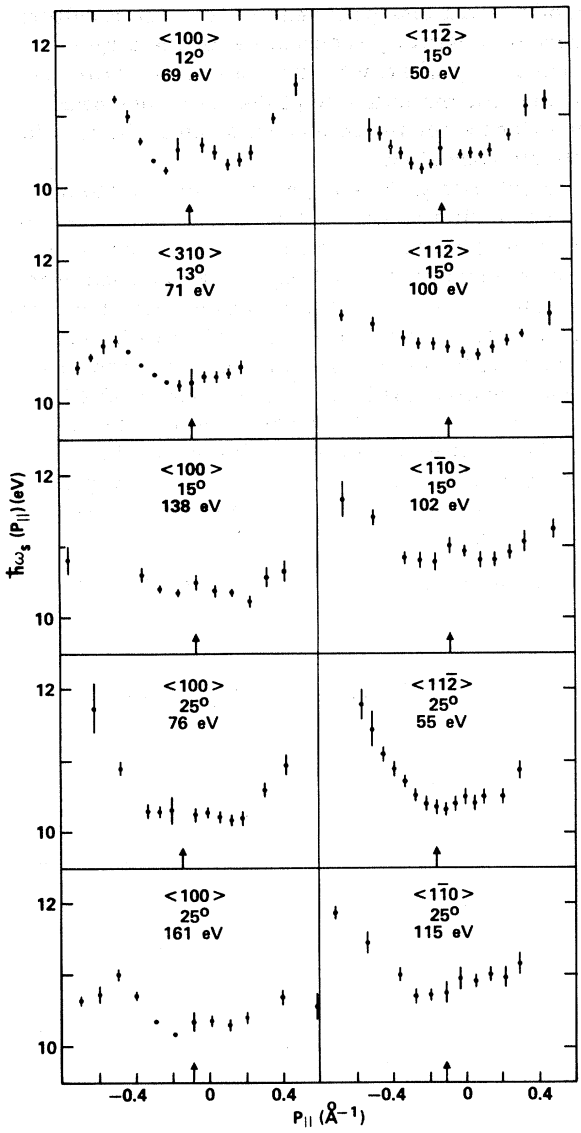

FIG. 16. SPDs obtained via the conservation law model from loss profiles where $E \simeq E_B$. Panels on the left represent single-crystal Al (001), and those on the right represent Al (111) data from I. Vertical arrows at the bottom of each panel indicate the specular condition, i.e., $\theta' = \theta$.

Equation (5b) is preferred to (5a) in view of the previously reported value of $\hbar\omega_s(0) = 10.5(\pm 0.1)$ for Al (111),[18,19] and a purely theoretical result,[30] based on the random-phase approximation, which implies that $\hbar\omega_s(0)$ is face independent. It is now realized that the uncertainty in the higher-order dispersion constants reported[18,19] for Al (111) is larger than previously estimated, because the kinematic character of the elastic energy profiles was not verified. The revised dispersion relationship for Al (111) may be expressed in the form[22]

$$\hbar\omega_s(p_\parallel) = 10.5(\pm 0.1) + C_1(\pm 0.5)p_\parallel + C_2(\pm 0.5)p_\parallel^2 , \tag{6a}$$

where

$$2.6\ C_1 + C_2 = 6.5;\quad C_2 > 0,\quad C_1 \gtrsim -1 \tag{6b}$$

and

$$\Gamma_s(p_\parallel) = 1.85(\pm 1) + 3(\pm 2)p_\parallel . \tag{6c}$$

The analysis based on the kinematic two-step model thus verifies the face dependence of the SPD obtained via the CLM. The ultimately positive character of the SPD on both surfaces is also verified. The latter result disagrees with the flat dispersion reported from high-energy electron forward-scattering measurements in polycrystalline foils.[11] However, when one considers the experimental uncertainty, in addition to the possible effects of

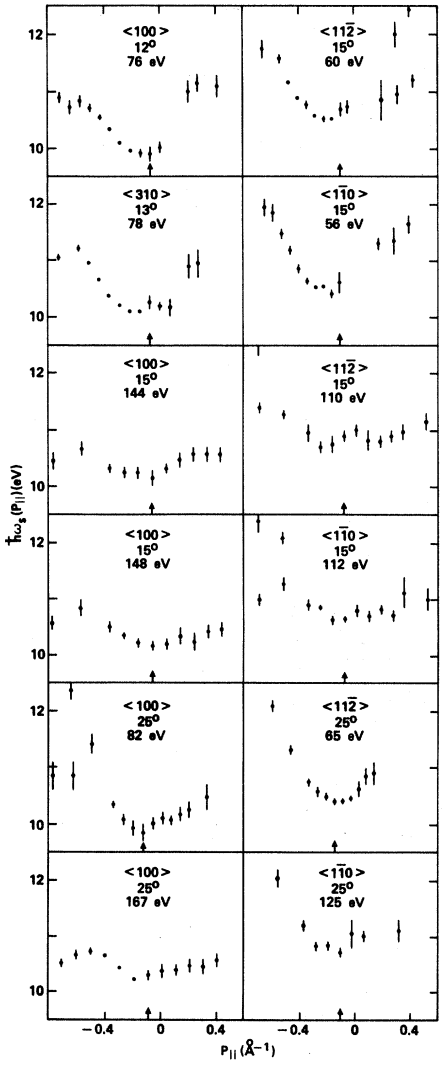

FIG. 17. SPDs similar to Fig. 16 for situations where $E > E_B$.

different effective surface geometry and structure, the disagreement seems not unreasonable. The values of $\hbar\omega_s(0)$ appearing in Eqs. (5b) and (6a), which should be independent of the (clean) surface characteristics,[30] are in fact in satisfactory agreement with the polycrystalline results.

The general conclusion from the kinematic two-step analysis is that the SPD is ultimately positive, face dependent, and somewhat "flatter" on the Al (001) surface than on Al (111), while the threshold $\hbar\omega_s(0)$ is substantially face independent. A possible interpretation is that this is a result of the looser packing of atoms on the Al (001) face which leads to a broader electron-density profile at the surface. Other influences may be important, however, as discussed elsewhere.[22]

VII. SUMMARY

ILEED measurements aimed at the determination of the surface-plasmon dispersion and lifetime have been extended to clean macroscopic single-crystal Al (111) and Al (001) surfaces. Surface cleanliness has been verified with *in situ* Auger analysis. Comparison with earlier measurements on an epitaxial Al (111) sample shows no significant dependence on sample type other than a lower incoherent background from the single-crystal sample. An extensive study of (00) beam elastic energy profiles from the Al (001) sample indicates stronger dynamical effects than previously realized, causing greater difficulty in finding conditions suitable for a kinematic ILEED analysis. Loss profiles measured near the specular direction on Al (001) occasionally show an extra peak lying between the surface, and bulk-loss peaks. On the basis of its appearance only at near-specular angles and only on the one face, the extra peak is attributed to a surface-related one-electron transition. Using the conservation law model, surface-plasmon dispersion relationships derived from the loss-profile data measured under different conditions show both systematic and individual inconsistencies resulting from the shortcomings of the model. Nevertheless, a general qualitative comparison of results from Al (001) with those from Al (111) is possible, and leads to the important conclusion that the dispersion is face-dependent and ultimately positive on both surfaces. An analysis based on a more sophisticated model, which is reported elsewhere,[22] supports and quantifies this conclusion. The present results appear not to be in serious disagreement with those based on high-energy electron scattering in polycrystalline foils[11] when experimental uncertainties and the possible effects of different surface structure and geometry are considered.

ACKNOWLEDGMENTS

We are grateful to Dr. C. B. Duke for many helpful and stimulating discussions and for a critical reading of the manuscript. We are also grateful to Dr. R. G. Musket for providing some of the Al crystals.

---

*Work supported in part by Navy Independent Research Funding and in part by the Defense Advanced Research Projects Agency under Order No. 2175.

[1]A. J. Bennett, Phys. Rev. B 1, 203 (1970).
[2]D. E. Beck and V. Celli, Surf. Sci. 37, 48 (1973); D. E. Beck, Phys. Rev. B 4, 1555 (1971).
[3]C. H. Hegener and D. Wagner, Z. Phys. 244, 499 (1971).
[4]J. Harris, J. Phys. C 5, 1757 (1972).
[5]J. Heinrichs, Phys. Rev. B 7, 3487 (1973); Solid State Commun. 12, 167 (1973).
[6]J. E. Inglesfield and E. Wikborg, Solid State Commun. 14, 661 (1974).
[7]P. J. Feibelman, Phys. Rev. B 9, 5077 (1974).
[8]C. J. Powell and J. B. Swan, Phys. Rev. 115, 869 (1959); 118, 640 (1960).
[9]C. Kunz, Z. Phys. 196, 311 (1966).
[10]T. Kloos, Z. Phys. 208, 77 (1968).
[11]T. Kloos and H. Raether, Phys. Lett. A 44, 157 (1973).
[12]T. Kloos, Z. Phys. 265, 225 (1973).
[13]S. Andersson, B. I. Lundqvist, G. Srinivasan, and E. Wikborg, Solid State Commun. 11, 1405 (1972); S. Andersson, Solid State Commun. 11, 1401 (1972).
[14]C. B. Duke and U. Landman, Phys. Rev. B 7, 1368 (1973).
[15]J. O. Porteus and W. N. Faith, J. Vac. Sci. Technol. 9, 1062 (1972).
[16]J. O. Porteus and W. N. Faith, Phys. Rev. B 2, 1532 (1970).
[17]M. P. Seah, Surf. Sci. 24, 357 (1971).
[18]C. B. Duke and U. Landman, Phys. Rev. B 8, 505 (1973).
[19]J. O. Porteus and W. N. Faith, Phys. Rev. B 8, 491 (1973).
[20]J. O. Porteus, Surf. Sci. 41, 515 (1974).
[21]J. Wendelken, Ph. D. thesis (University of Illinois, 1974); Coordinated Science Laboratory Report R-667; Phys. Rev. (to be published).
[22]C. B. Duke, L. Pietronero, J. Porteus, and J. Wendelken, Phys. Rev. B (to be published).
[23]C. B. Duke, U. Landman, and J. O. Porteus, J. Vac. Sci. Technol. 10, 183 (1973).
[24]C. B. Duke and U. Landman (unpublished).
[25]The term $(2n\Delta w)^{-1}$ which appears on the left-hand sides of Eqs. (I1) and (I2), and also in the text of I, is in error and should be replaced by $n\Delta w/2$.
[26]See, e.g., Fig. 1 of Ref. 15.
[27]C. B. Duke and U. Landman, Phys. Rev. B 6, 2968 (1972).
[28]A. Bagchi and C. B. Duke, Phys. Rev. B 5, 2784 (1972).
[29]C. B. Duke, private communication.
[30]P. J. Feibelman, Phys. Rev. B 2, 220 (1970).